

Spiral stellar density waves and the flattening of abundance gradients in the warm gas component of spiral galaxies.

E. I. Vorobyov ^{*}

¹ *CITA National Fellow, Department of Physics and Astronomy, University of Western Ontario, London, Ontario, N6A 3K7, Canada.*

7 May 2017

ABSTRACT

Motivated by recent observations of plateaus and minima in the radial abundance distributions of heavy elements in the Milky Way and some other spiral galaxies, we propose a dynamical mechanism for the formation of such features around corotation. Our numerical simulations show that the non-axisymmetric gravitational field of spiral density waves generates cyclone and anticyclone gas flows in the vicinity of corotation. The anticyclones flatten the pre-existing negative abundance gradients by exporting many more atoms of heavy elements outside corotation than importing inside it. This process is very efficient and forms plateaus of several kiloparsec in size around corotation after two revolution periods of a galaxy. The strength of anticyclones and, consequently, the sizes of plateaus depend on the pitch angle of spiral arms and are expected to increase along the Hubble sequence.

Key words: ISM:abundances - galaxies:abundances - galaxies:spiral

1 INTRODUCTION

It has recently been recognized that density waves in the stellar component of spiral galaxies have a profound effect on the dynamics of stars, cold gas clouds, and dust in the vicinity of the corotation resonance. The non-axisymmetric gravitational field of spiral stellar density waves causes large changes (~ 50 per cent over the lifetime of a galaxy) in the angular momenta of individual stars and cold gas clouds around the corotation radius (Sellwood & Binney 2002). Considerable radial migrations associated with the angular momentum changes are expected to dilute the abundance gradients in the cold gas component of spiral galaxies (Sellwood & Preto 2002).

The radial abundance distribution of heavy elements in log scale in at least some spiral galaxies (perhaps, including the Milky Way) cannot be described by a linear function with a negative slope. According to Zaritsky, Kennicutt, & Huchra (1994), the oxygen abundances in NGC 2997, NGC 3319, NGC 5033 and other spiral galaxies in their sample show a complex nonlinear behaviour – plateaus and minima can be identified in the radial distribution of oxygen. Perhaps more convincing evidence for a complex radial distribution of heavy element abundances is found in the Milky Way. For instance, the radial abundance distributions of O, N, Mg, and other heavy elements derived by Daflon & Cunha (2004) from a sample of OB stars show a minimum near 8 kpc (although they have not accentuated the impor-

tance of this behaviour and approximated the radial abundance profiles by a linear function with a negative slope). The existence of a plateau in the oxygen abundance distribution has also been reported by Andrievsky et al. (2002). Although a definite confirmation of plateaus or/and minima in the radial abundance profiles of heavy elements requires a larger sample of abundance tracers than has been used in the abovementioned studies, the existing evidence strongly suggests these features.

A simple multizone model of chemical enrichment in spiral galaxies has been recently proposed by Mishurov et al. (2002) and Acharova et al. (2005). It explains the formation of minima and/or plateaus in the radial abundances of heavy elements near corotation by a selective action of star formation. The star formation rate around corotation is assumed to have a minimum (due to the lack of strong spiral shock waves) and consequently the heavy element production also has a minimum at the corotation radius. The assumed temporal migration of the corotation resonance can produce either plateaus or minima in the radial abundance distributions of heavy elements.

In this paper, we focus on a purely hydrodynamic explanation for a nonlinear radial distribution of heavy elements in spiral galaxies. We present the first numerical hydrodynamic simulations that self-consistently explain the formation of a plateau in the heavy element abundance distribution in the vicinity of corotation. We demonstrate the development of cyclones and anticyclones in the gas flow around corotation and study their influence on the radial abundance distribution of heavy elements in spiral galaxies.

* E-mail: vorobyov@astro.uwo.ca (EIV)

The existence of cyclones and anticyclones has been observationally confirmed in at least two spiral galaxies (Fridman et al. 2001a; 2001b) and has been predicted in the laboratory experiments of rotating shallow water modelling (Nezlin 1994). The model equations are formulated in § 2. The numerical code is described in § 3 and the initial conditions are given in § 4. The results of numerical simulations are presented in § 5. The possible implications for spiral galaxies of different Hubble types are discussed in § 6. The main results are summarized in § 7.

2 MODEL DESCRIPTION AND BASIC EQUATIONS

Our model galaxy consists of a gas disk that evolves in the external gravitational potential of the spherical dark matter halo and stellar disk. We study the behaviour of the warm gas component ($T \sim 10^4$ K) and the heavy element admixtures within it, which can be adequately described by the equations of hydrodynamics. The stellar disk is split into axisymmetric and non-axisymmetric components. The axisymmetric component is assumed to have a power-law radial density profile, whereas the non-axisymmetric component is described by a running spiral density wave (Lin et al. 1969). The density profile of the spherical dark matter halo is assumed to be that of a modified isothermal sphere (Binney & Tremaine 1987).

We use the physically motivated thin-disk approximation to describe the motion of gas and heavy elements in the external gravitational potential of the dark matter halo and stellar disk. In this approximation, the radial extent of the gas disk is assumed to be much larger than its vertical height, discarding the need to solve for the vertical motion of gas. We assume that heavy elements are collisionally coupled to the gas, which eliminates the need to solve the equations of motion for the heavy elements. The basic equations governing the dynamics of the gas and heavy element components are

$$\frac{\partial \Sigma_x}{\partial t} = -\nabla \cdot (\mathbf{v} \Sigma_x), \quad (1)$$

$$\frac{\partial \Sigma_g}{\partial t} = -\nabla \cdot (\mathbf{v} \Sigma_g), \quad (2)$$

$$\frac{\partial \mathbf{v}}{\partial t} + (\mathbf{v} \cdot \nabla) \mathbf{v} = -\nabla \Phi_{s1,s2,h} - \frac{\nabla P}{\Sigma_g}. \quad (3)$$

Here, Σ_g and Σ_x are the surface densities of the gas and heavy element components, respectively, \mathbf{v} is the gas velocity in the disk plane, and $P = c_s^2 \Sigma$ is the vertically integrated gas pressure. The gas disk is assumed to be isothermal at $T = 10^4$ K, which yields a value of $c_s = 9.12$ km s⁻¹ for the isothermal sound speed. We note that if the ratio Σ_x/Σ_g is constant in the disk at any given time, it will continue to be constant at all times, because Σ_x will be advected exactly in the same manner as Σ_g . The expressions for the gravity force due to the gravitational potentials Φ_h , Φ_{s1} , and Φ_{s2} of the dark matter halo, axisymmetric and non-axisymmetric stellar components, respectively, are given below.

The spherical dark matter halo has a density profile described by the modified isothermal sphere

$$\rho_h = \frac{\rho_{h0}}{(1 + r/r_h)^2}, \quad (4)$$

where ρ_{h0} and r_h are the central volume density and characteristic scale length of the dark matter halo, the values of which are fixed by the halo mass M_h as described in Vorobyov & Shchekinov (2006) and references therein. In the following text we assume $M_h = 10^{12} M_\odot$. The radial gravity force of the spherical dark matter halo in the plane of the gas disk can be written as

$$\frac{\partial \Phi_h}{\partial r} = 4\pi G \rho_{h0} r_h [r/r_h - \arctan(r/r_h)] \left(\frac{r_h}{r}\right)^2. \quad (5)$$

The axisymmetric component of the stellar disk is assumed to have a power-law radial density profile of the form

$$\Sigma_s(r) = \frac{B^2}{2\pi G} [(r_s^2 + r^2)^{-3/2}], \quad (6)$$

where $B^2 = 2\pi G r_s^3 \Sigma_{s0}$. The radial component of the gravity force of such a density distribution is given by Toomre (1963)

$$\frac{\partial \Phi_{s1}}{\partial r} = B^2 \left[\frac{r}{r_s} (r_s^2 + r^2)^{-3/2} \right]. \quad (7)$$

In the following, we use the central stellar density $\Sigma_{s0} = 1.2 \times 10^3 M_\odot \text{ pc}^{-2}$ and $r_s = 3$ kpc, which gives us a total stellar mass of $M_{st} = 7 \times 10^{10} M_\odot$.

The non-axisymmetric part of the stellar gravitational potential is described in the polar coordinates (r, ϕ) by a running density wave as (Lin et al. 1969, Lépine et al. 2003, Vorobyov & Shchekinov 2006)

$$\Phi_{s2}(r, \phi) = -C(r) \cos [m(\cot(i) \ln(r/r_{sp}) + \phi - \Omega_{sp}t)], \quad (8)$$

where $C(r)$ is the radially varying amplitude of the stellar gravitational potential, i is the pitch angle, r_{sp} is the characteristic radius of the spiral at $\phi = 0$, m is the number of spiral arms, and Ω_{sp} is the angular velocity of spiral pattern. In the following we adopt $m = 2$, $r_{sp} = 6$ kpc and $\Omega_{sp} = 21$ km s⁻¹ kpc. The value of i is varied to study its influence on the radial distribution of heavy elements. Care should be taken when choosing the amplitude $C(r)$ to avoid unphysically large azimuthal gravity forces near the origin. The reader is referred to Vorobyov & Shchekinov (2006) for a detailed discussion on this subject.

3 CODE DESCRIPTION

An Eulerian finite-difference code is used to solve equations (1)-(3) in the polar coordinates (r, ϕ) . The basic algorithm of the code is similar to that of the ZEUS code presented by Stone & Norman (1992). The operator splitting is utilized to advance in time the dependent variables in two coordinate directions. The advection is treated using the consistent transport method of Stone and Norman and the van Leer interpolation scheme. The resolution is 400×400 grid points and the radial size of the grid cell is 50 pc. The code performs well on the angular momentum conservation problem (Norman et al. 1980). This test problem is essential for the adequate modelling of rotating systems with radial mass transport.

4 INITIAL CONFIGURATION

The initial equilibrium gas disk configuration is initialized by fixing the radial profile of the gas disk and calculating

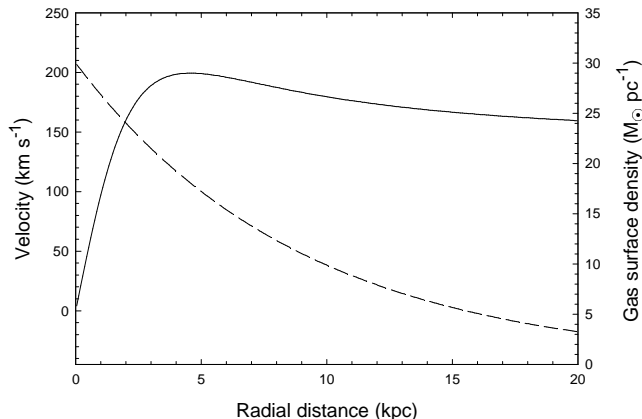


Figure 1. The initial rotation curve (solid line) and gas surface density distribution (dashed line).

the rotation curve that balances the combined gravity force of the dark matter halo and axisymmetric part of the stellar disk. We assume that the gas disk has an exponentially declining density profile

$$\Sigma_{\text{g}} = \Sigma_{\text{g}0} \exp(-r/r_{\text{g}}), \quad (9)$$

with the central surface density $\Sigma_{\text{g}0} = 30 M_{\odot} \text{ pc}^{-2}$, and radial scale length $r_{\text{g}} = 9 \text{ kpc}$. The total mass of the gas disk within the computational domain ($r = 20 \text{ kpc}$) is $M_{\text{g}} = 1.0 \times 10^{10} M_{\odot}$. Hence, the gas disk contains only a small fraction ($\sim 10\%$) of the total mass in the computational domain and, to a first approximation, we can neglect its self-gravity. The initial gas density profile and the initial rotation curve are shown in Fig. 1 by the dashed and solid lines, respectively.

Once the equilibrium gas disk is set, we slowly introduce the non-axisymmetric part of the stellar disk. Specifically, $\Phi_{\text{s}2}$ is multiplied by a function $\epsilon(t)$, which has a value of 0 at $t = 0$ and linearly grows to its maximum value of 1.0 at $t \geq 200 \text{ Myr}$. It takes a few hundred Myr for the gas disk to adjust to the spiral distortion and develop a spiral structure.

We do not attempt to follow the exact chemical evolution of our model galaxy. Instead, we simply assume that at the time when spiral structure appears the model galaxy has already developed the abundance of elements that is typical for disk galaxies. We further focus on the purely dynamical influence of stellar spiral density waves on the distribution of pre-existing heavy elements in the galactic disk. Taking the above considerations into account, we construct the radial distribution of heavy elements by assuming that they have a given abundance at corotation and choose an appropriate negative radial gradient. The effect of star formation will be considered in a subsequent paper.

5 RADIAL MIGRATIONS OF HEAVY ELEMENTS AT COROTATION

As was demonstrated by Sellwood & Binney (2002) and Vorobyov & Shchekinov (2006), spiral stellar density waves at corotation are powerful drivers of radial migration of stars and dust. In this section, we study the effect that spiral density waves have on the radial abundance distribution of

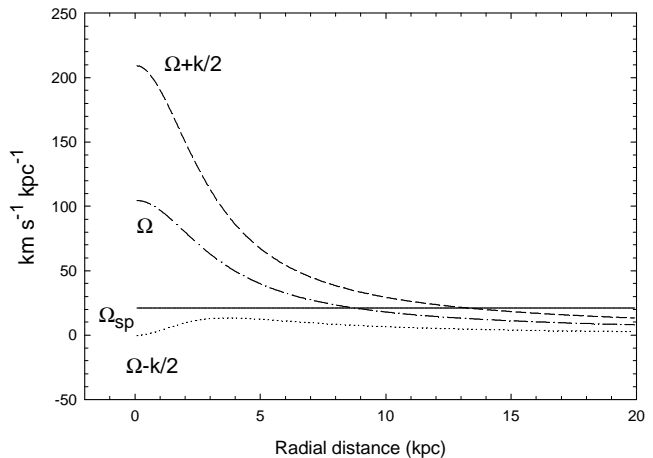


Figure 2. Radial profiles of the gas angular velocity Ω (dotted-dashed line) and $\Omega \pm k/2$ (dashed and dotted lines, respectively), where k is the epicyclic frequency. The angular velocity of spiral pattern Ω_{sp} is shown by the solid line.

heavy elements in the warm gas component of spiral galaxies. Two models of spiral stellar density waves are considered. In both models, the stellar density wave (the gravitational potential of which is given by Eq. [8]) rotates counter clockwise at an angular velocity $\Omega_{\text{sp}} = 21 \text{ km s}^{-1} \text{ kpc}^{-1}$. This choice of Ω_{sp} places the corotation of the gas disk at $\approx 9 \text{ kpc}$ and the outer Lindblad resonance at $\approx 13 \text{ kpc}$ as is shown in Fig. 2. The inner Lindblad resonance is absent. The pitch angle is $i = 25^\circ$, if not otherwise stated. According to Kennicutt (1981), a pitch angle of $i = 25^\circ$ is typical for Sc galaxies. The radial position of resonances may vary along the azimuth during the evolution of the gas disk by $\approx 5\%$.

In the first model (hereafter, model 1), the amplitude of the stellar spiral gravitational potential $C(r)$ is chosen so that it is maximal near the position of corotation. Consequently, the gas disk has a strong spiral response to the underlying spiral stellar density wave at both sides of corotation. In the second model (hereafter, model 2), the spiral stellar density wave is mostly localized within corotation. Observationally, models 1 and 2 represent two types of spiral galaxies in which corotation is situated approximately in the middle of the spiral pattern and at the very end of it, respectively.

Since we do not consider the effect of star formation on the abundance distribution of heavy elements, we choose not to focus on any particular element like oxygen or iron but instead use an abundance of a generic heavy element X defined as

$$\left[\frac{X}{H} \right] = \log_{10} \left(\frac{\Sigma_{\text{X}}}{\Sigma_{\text{g}}} \right) - \log_{10} \left(\frac{\Sigma_{\text{X}}}{\Sigma_{\text{g}}} \right)_{\text{cr}}. \quad (10)$$

The last term in equation (10) gives the abundance of heavy element X at corotation. In the following, we assume that element X has an initial radial abundance gradient of $-0.05 \text{ dex kpc}^{-1}$. According to Daflon & Cunha (2004), an average radial slope of such elements as C, N, O, Mg, Al, Si, and S in the Galactic disk is $-0.042 \pm 0.007 \text{ dex kpc}^{-1}$. The oxygen abundance in a sample of external galaxies studied by Zaritsky, Kennicutt, & Huchra (1994) shows a

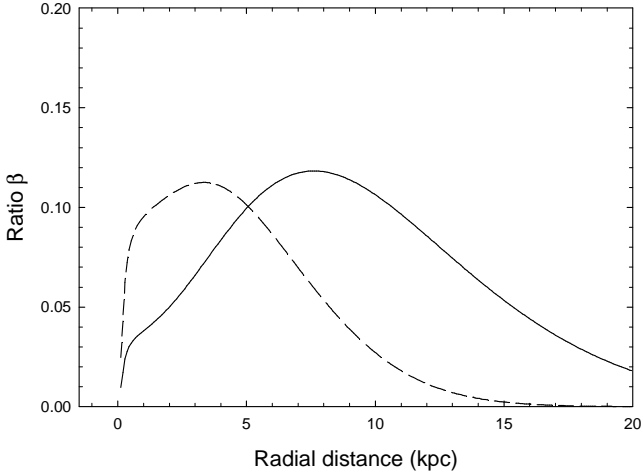


Figure 3. The ratio β of the maximum non-axisymmetric gravitational acceleration (at a given radial distance r) $|\nabla\Phi_{s2}| = [(\partial\Phi_{s2}/\partial r)^2 + (r^{-1}\partial\Phi_{s2}/\partial\phi)^2]^{1/2}$ to the total axisymmetric gravitational acceleration $|(\partial\Phi_{s1}/\partial r + \partial\Phi_h/\partial r)|$ as a function of radial distance in model 1 (solid line) and model 2 (dashed line).

wide spread in the radial slopes ranging from -0.009 ± 0.01 dex kpc^{-1} for NGC 1365 to -0.231 ± 0.022 dex kpc^{-1} for NGC 3344 (some galaxies have a positive slope). On average, most galaxies in their sample have radial oxygen gradients near -0.05 dex kpc^{-1} . Once the radial abundance gradient and the abundance at corotation are fixed, we can use equation (10) to determine Σ_x and equations (1)-(3) to compute the dynamics of the gas and heavy element X.

5.1 Model 1

The amplitude $C(r)$ of the spiral stellar gravitational potential determines the response of the gas and consequently the appearance of a spiral pattern in the gas disk. We adopt the following expression $C(r) = C_0(r)^{\alpha(r)}$. Here, $C_0(r)$ is a linear function of r which has a value of 0 at $r = 0$ kpc and attains its maximum value of 0.0018 (in dimensionless units) at $r = 20$ kpc. The exponent $\alpha(r)$ decreases linearly with radius from $\alpha = 2$ at $r = 0$ kpc to $\alpha = -0.1$ at $r = 20$ kpc. The resulting ratio $\beta(r)$ of the maximum non-axisymmetric gravitational acceleration $|\nabla\Phi_{s2}|$ (at a given radial distance r) to the total axisymmetric gravitational acceleration $|(\partial\Phi_{s1}/\partial r + \partial\Phi_h/\partial r)|$ is shown in Fig. 3 by the solid line. Since the non-axisymmetric gravitational acceleration scales as $|\nabla\Phi_{s2}| \propto 1/r^{1-\alpha(r)}$, the ratio β increases with radius at $r < 7.5$ kpc, and decreases at $r \gtrsim 7.5$ kpc. We note that the maximum, non-axisymmetric perturbing force never exceeds 12% of the total axisymmetric gravity force. At the position of corotation $r_{\text{cr}} \approx 9$ kpc, β approximately equals 11%.

Once the spiral stellar density wave is slowly turned on, the initially axisymmetric gas disk responds to a disturbing gravitational field of stellar spirals and develops a spiral pattern. The left panels of Fig. 4 show the evolution of the gas surface density at two different times as indicated in each panel. The two-arm spiral structure in the gas disk is clearly visible in these images. A strong gas response to the gravitational field of the spiral density wave is seen inside and outside corotation, the position of which is sketched by

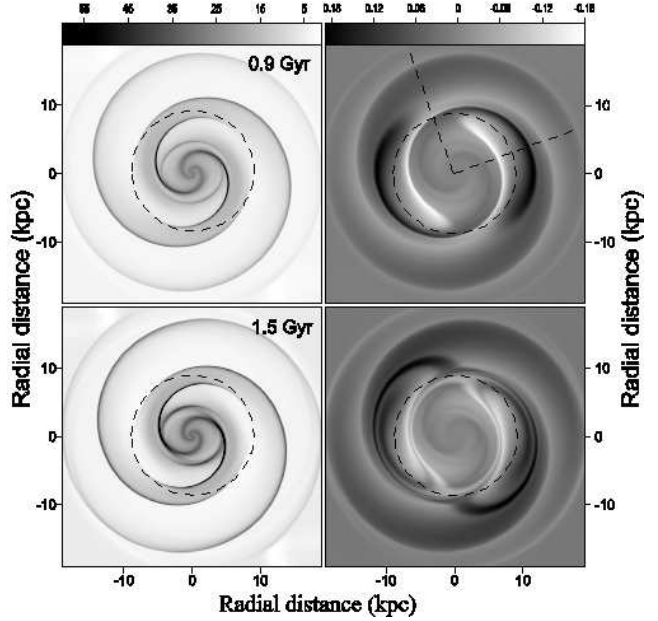


Figure 4. Left panels – the gas surface density distribution, right panels – the distribution of residual abundances of element X at two different evolutionary times as indicated in the left panels. The approximate position of corotation is shown by the dashed circle. The left scale bar is in $M_{\odot} \text{pc}^{-2}$ and the right scale bar is in dex.

a dashed circle. Enhancements and depressions in the gas surface density distribution by approximately a factor of 2 as compared to the unperturbed distribution are seen in the spiral arms and between them, respectively. The gas response to the spiral stellar density wave is minimal around corotation.

The right panels in Fig. 4 show the residual abundances $[X/H]_{\text{res}}$, which are obtained by subtracting the current abundances $[X/H]$ at a given position in the disk from those at $t = 0$ Gyr. If there were no radial and/or azimuthal migrations of element X due to spiral stellar density waves, the residual abundance would be zero during the consequent evolution of the gas disk. However, a considerable redistribution of element X near corotation is evident in Fig. 4 as indicated by large deviations of $[X/H]_{\text{res}}$ from zero. The maximum deviations of ± 0.18 dex are found between the spiral arms, whereas the deviation is noticeably smaller in the region where spiral arms cross corotation. This implies that the radial profiles of $[X/H]$ may be different along different radial directions. Indeed, Fig. 5 shows the radial distribution of $[X/H]$ along two radial cuts that are plotted by the dashed lines in the upper-right panel of Fig. 4. The first cut (hereafter, the upper cut) is made through the point in the disk where the gas spiral arms cross the corotation circle. The second cut (hereafter, the right cut) is made at a 90° angle to the upper cut. The initial axisymmetric abundance distribution of element X is plotted by the dotted line for comparison. An obvious (and impressive) difference is seen between the radial $[X/H]$ profiles along the upper and right cuts. The former shows a sharp drop near the position of corotation at $r \approx 9$ kpc, while the latter has a plateau (with a size of approximately 4 kpc) at the position of corotation. The radial profiles of $[X/H]$ inside corotation demonstrate

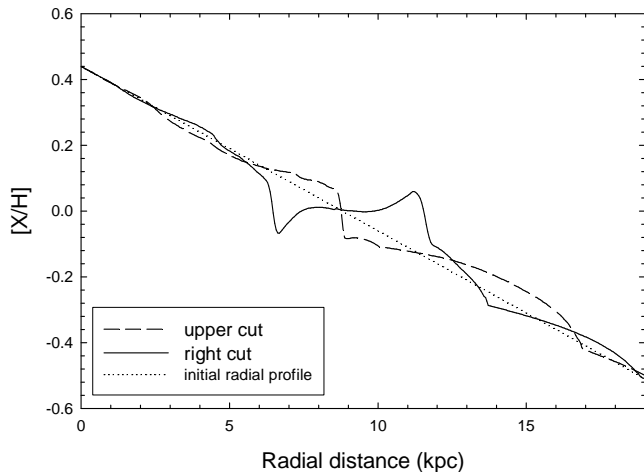


Figure 5. The radial abundance distribution of element X determined at $t = 0.9$ Gyr along two radial cuts made through the gas disk. The directions of the right and upper cuts are shown in the upper panel of Fig. 4 by the dashed lines. The dotted line shows the initial axisymmetric abundance distribution of element X.

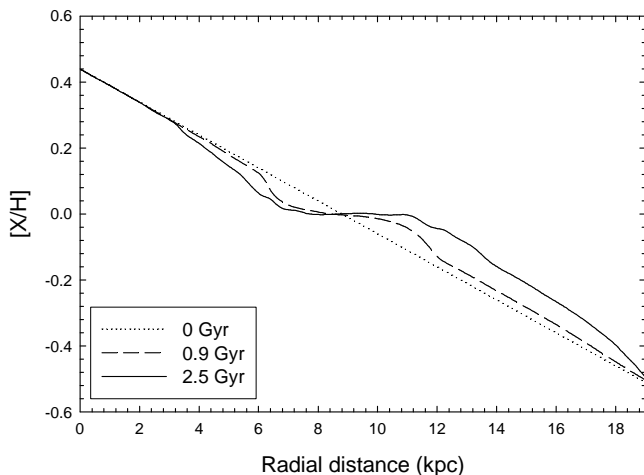


Figure 6. Azimuthally averaged abundance distribution of element X at three different times as indicated in the legend. The development of a plateau on both sides of corotation (≈ 9 kpc) is evident.

substantially smaller deviations from the initial axisymmetric radial profile, which implies little redistribution of heavy elements in the inner galactic regions.

A small number of metallicity indicators (such as HII regions or planetary nebula) usually makes it difficult to determine the radial abundance profiles along a particular radial direction in a galaxy. In this respect, the azimuthally averaged radial abundance distribution is of particular interest. The azimuthally averaged radial distribution of $[X/H]$ is shown in Fig. 6 at two different times after the beginning of simulations. The dotted line plots the initial axisymmetric abundance distribution of element X. The development of a plateau in the azimuthally averaged profiles of $[X/H]$ is evident in Fig. 6. Taking into account that the spiral perturbing force saturates after 200 Myr from the beginning of simulations, only two revolution periods (~ 640 Myr) are needed to develop a significant plateau with a size of 3 kpc. The

plateau grows in time and reaches a size of approximately 4.5 kpc after 2.5 Gyr. The radial redistribution of element X with respect to hydrogen is also visible in the plots – a substantial amount of element X (approximately 7% by mass) is pushed radially away in the disk by the action of spiral stellar density waves.

As was mentioned in the Introduction, the gravitational field of the stellar spiral arms is known to radially mix the stars and cold molecular clouds and transport dust radially away in the disks of spiral galaxies (Sellwood & Binney 2002, Vorobyov & Shchekinov 2006). In order to understand the effect that the stellar spiral arms have on the distribution of heavy elements in the warm gas phase of spiral galaxies, we consider a large-scale gas flow in the disk of our model galaxy. Figure 7 shows the residual velocity field of gas superimposed on the gas surface density distribution at $t = 0.9$ Gyr. The residual velocity field of the gas is obtained by subtracting the circular motion of gas due to the combined axisymmetric gravitational potential of stars and dark matter halo from the total gas velocity. The residual velocity field shows a complicated flow pattern. However, several regular features of the gas flow are clearly visible in Fig. 7. On average, the gas streams radially inward along the outer edge of a spiral arm and radially outward along the inner edge. The radial velocities are considerable and may become as high as $\pm(25 - 30)$ km s $^{-1}$ near the corotation circle. These large-scale radial gas motions are caused by the gravitational field of stellar spiral density waves. A hydrogen atom (as well as any other element coupled to hydrogen) is exposed to an additional gravitational attraction of the stellar density wave when it approaches the spiral arm. If the atom is closer to the concave part of the spiral, it will be pushed radially outward. On the other hand, if the atom is closer to the convex part of the spiral, it will be given an inward radial pull. This two-fold action of the spiral stellar density wave on the dynamics of a single particle is schematically depicted by Vorobyov & Shchekinov (2006) in their fig. 6. The gravitational field of stellar spirals can cause a considerable change in the angular momentum of a particular element (it could be either a gas parcel or a star) but the total angular momentum of the system remains largely unchanged.

The effect of spiral stellar density waves on the dynamics of gas (and heavy element admixtures within it) is strongest around the corotation resonance, where a gas parcel *rotates in phase with the stellar spiral density wave* and is subject to the maximal radial migrations. Considerably away from corotation, the gas parcel frequently passes through the spiral arms and the gravitational influence of the latter mostly cancels out (as is seen in the trajectories of test particles in Fig. 5 of Vorobyov & Shchekinov 2006). The net result of the radial migrations of heavy elements is a flattening of the pre-existing negative radial abundance gradients near corotation. Since the abundance of element X is larger inside corotation than outside it, the radial gas flow exports many more atoms of element X outside corotation than it takes from there. This process continues until a near homogeneous abundance distribution is set on both sides of corotation.

The smearing of negative abundance gradients near corotation can be better understood in terms of anticyclones that develop between the spiral arms and are sketched in

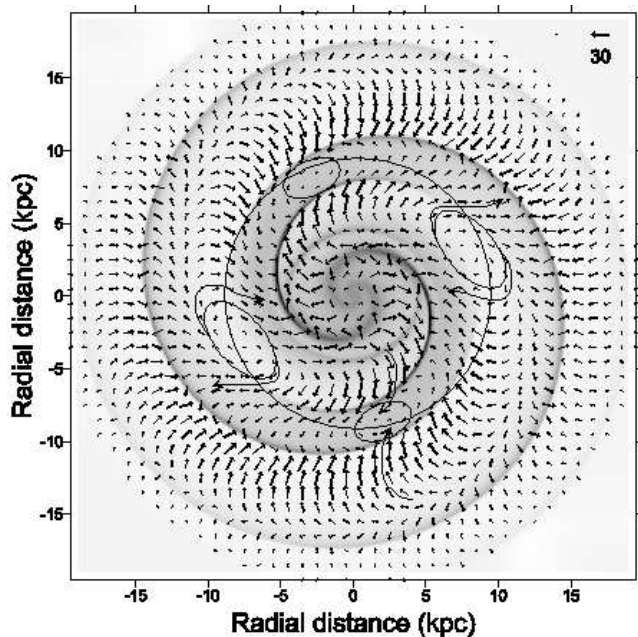


Figure 7. The residual gas velocity field superimposed onto the gas surface density distribution in model 1 at $t = 0.9$ Gyr. The locations of cyclones and anticyclones are shown with the smaller and larger ellipses, respectively. Large arrows sketch the gas flow in cyclones and anticyclones. Corotation is drawn by the circle. The scale vector is in km s^{-1} .

Fig. 7 by the larger ellipses. The anticyclone flow of gas is approximately shown by the long arrows. It is clearly seen that the anticyclones push the gas from inside corotation to the regions outside it and vice versa, thus producing an effective mixing of elements and flattening of negative abundance gradients at the position of anticyclones (i.e. between the spiral arms). The small ellipses show the location of two cyclones that form in the disk near the point where spiral arms cross the corotation circle. Two approaching streams of gas in the cyclone (shown by the long arrows in Fig. 7) meet near corotation, which creates a contact discontinuity and a subsequent sharp drop in the abundance distribution at corotation. Such a step-like feature is clearly seen in the radial abundance distribution of element X calculated along the radial cut that passes through the position of the cyclone (see the dashed line in Fig. 5).

The formation of cyclones and anticyclones in the gas disk is a consequence of a non-axisymmetric gravitational field of the stellar spiral density wave. A gas parcel that orbits sufficiently close to corotation ($\lesssim 2$ kpc on both sides of it) is exposed to a strong resonant forcing of the spiral gravitational field. Such resonant forcing produces anticyclones and associated considerable radial migrations of gas and heavy elements. An example of trajectories around corotation is shown by the solid line in Fig. 5 of Vorobyov & Shechkinov (2006). The same type of “horse-shoe” orbit was found by Sellwood & Binney (2002) in a stellar disk around corotation. We note that the existence of such cyclone and anticyclone motions was indeed revealed in the gas disks of NGC 3631 (Fridman et al. 2001a) and NGC 157 (Fridman et al. 2001b). The anticyclone motions of cold gas clouds

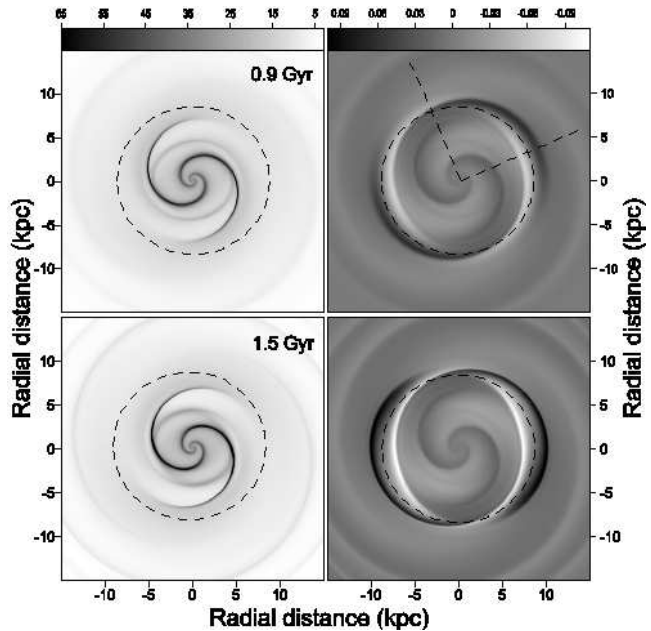


Figure 8. The same as Figure 4 but for model 2.

around corotation in spiral galaxies were also suggested by Sellwood & Preto (2002).

Another important implication seen in Fig 7 is that the gas *is not pushed away from corotation everywhere along the corotation perimeter*. An assumption of the outflow of gas away from corotation usually involves a two-fold effect of spiral shocks (triggered by stellar density waves) on the gas that passes through the shock front. Because of differential rotation, the gas that orbits inside/outside corotation is decelerated/accelerated at the shock front and is driven radially inward/outward from corotation. This conclusion may be misleading because it completely neglects the long-range influence of the gravitational field of spiral arms, which appear to have a much stronger effect on the gas dynamics than the spiral shock fronts. The gas is indeed pushed away from corotation by the action of anticyclones but is returned to corotation by the action of cyclones. However, the azimuthally averaged gas surface density distribution shows a mild gas depression near corotation as compared to the initial distribution, implying that anticyclones are more powerful than cyclones.

5.2 Model 2

Simulations of the previous section have shown that the spiral stellar density waves induce anticyclone flows of gas near corotation and, by doing so, flatten the pre-existing negative abundance gradients of heavy elements in the warm gas. This effect is limited to several kiloparsecs on each side of corotation, and the abundance distribution retains (on average) its initial slope at radial distances that are considerably far from corotation. This implies that if the stellar spirals are entirely confined within corotation, we should not expect to see a considerable flattening of the negative abundance gradients. We check this assumption by considering model 2 in which we choose the amplitude $C(r)$ of the spiral stellar gravitational potential so that the stellar density waves are

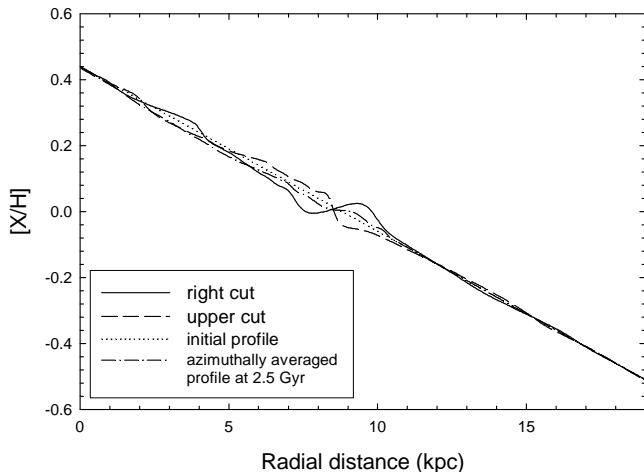


Figure 9. The radial abundance distribution of element X determined at $t = 0.9$ Gyr along two radial cuts made through the gas disk. The directions of the right and upper cuts are shown in the upper panel of Fig. 8 by the dashed lines. The dotted line shows the initial axisymmetric abundance distribution of element X. The dashed-dotted line shows the azimuthally averaged abundance distribution at $t = 0.9$ Gyr.

mostly localized within corotation. This means that they have a negligible effect on the gas dynamics outside corotation. The same expression for the amplitude $C(r)$ as in model 1 is adopted. However, the exponent $\alpha(r)$ decreases linearly with radius from $\alpha = 2$ at $r = 0$ kpc to $\alpha = -2.4$ (in contrast to $\alpha = -0.1$ in model 1) at $r = 20$ kpc. The resulting profile of the maximum non-axisymmetric gravitational acceleration to the total axisymmetric gravitational acceleration $\beta(r)$ is shown in Fig. 3 by the dashed line. The ratio β increases with radius at $r < 4$ kpc, and decreases at $r \gtrsim 4$ kpc. We note that the maximum, non-axisymmetric gravitational acceleration never exceeds 11% of the total axisymmetric gravity force. At the position of corotation $r_{\text{cr}} \approx 9$ kpc, β approximately equals 4% and it sharply decreases beyond corotation.

The left panels in Fig. 8 show the evolution of the gas surface density at two different times as indicated in each panel. The gas response to the gravitational field of spiral stellar density waves in model 2 is remarkably different from that of model 1. The gas spiral pattern in model 2 is completely localized within corotation, which is drawn in Fig. 8 by a dashed circle. A weak spiral structure can be traced in the gas disk beyond corotation but its amplitude is negligible compared to that inside corotation. The right panels in Fig. 8 show the distribution of residual abundance $[X/H]_{\text{res}}$. The maximum deviations from the initial abundance distribution of element X are found near corotation. However, they are (at least) a factor of 2 smaller than in model 1. As in the previous section, we make two radial cuts in the gas disk at $t = 0.9$ Gyr and calculate the abundance profiles of element X along these cuts. The cuts are drawn in the upper-left panel of Fig. 8 by the dashed lines. The directions of the cuts are the same as in model 1, which allows for a direct comparison between both models. The solid and dashed lines in Fig. 9 show the resulting distributions of $[X/H]$ obtained along the upper and right cuts, respectively. The dotted line shows the initial $[X/H]$ distribution for comparison.

It is obvious that the deviation from the initial unperturbed axisymmetric distribution is much smaller in model 2 than in model 1. The abundance profiles do have a small plateau and a mild discontinuity at the position of corotation, but this effect is mostly cancelled out after azimuthal averaging. As a result, the azimuthally averaged abundance distribution of element X plotted in Fig. 9 by the dashed-dotted line is almost indistinguishable from the initial unperturbed distribution.

The difference between the two models in the efficiency of flattening of element abundance gradients can be readily understood if we consider the residual gas velocity field which is obtained by subtracting the circular velocity of gas (due to the axisymmetric gravitational field) from the total gas velocity. Figure 10 presents the residual gas velocity field superimposed onto the gas surface density distribution at $t = 0.9$ Gyr. The approximate position of corotation is drawn by the dashed line. Similarities and differences in the overall gas flow in model 1 and model 2 are evident. In both models, the gas streams inward/outward along the outer/inner edges of spiral arms. However, in model 2 the radial velocities around corotation are at least an order of magnitude smaller ($\approx 2 - 3 \text{ km s}^{-1}$) than in model 1. Very weak cyclones and anticyclones are seen around corotation. Inside corotation ($r < 7$ kpc), considerable radial velocities up to 35 km s^{-1} are evident in Fig. 10. Nevertheless, these radial flows involve little radial transport of heavy elements (and consequent flattening of negative abundance gradients), because gas particles frequently cross the spiral arms and effectively cancel out the gravitational influence of the latter. As a result, gas particles and heavy element admixtures move around the galactic centre on closed low-eccentricity circular orbits, as shown by the dashed line in Fig. 5 of Vorobyov & Shchekinov (2006).

6 FLATTENING OF ABUNDANCE GRADIENTS ALONG THE HUBBLE SEQUENCE

The tightness of the spiral pattern defined by the pitch angle of spiral arms is one of the fundamental criteria in Hubble's (1926) classification scheme of spiral galaxies. Kennicutt (1981) has confirmed that there exist a correlation between the pitch angle and the Hubble type of spirals. A smooth, monotonic increase in the openness of spiral arms with later Hubble type is detected on the average, but large variations in the pitch angle within a given type are still present.

In the previous section, we studied open spirals with a pitch angle of $i = 25^\circ$. According to Kennicutt (1981), this value is near the upper limit ($i \approx 30^\circ$) for the late-type Sc galaxies. In this section, we consider more tightly-wound spirals typical for the early-type Sa-Sb galaxies. The model galaxy has the same initial parameters as model 1 of Sect. 5.1 but a pitch angle $i = 10^\circ$. The resulting azimuthally averaged radial abundance profiles of element X are plotted in Fig. 11 at two different evolutionary times. The initial radial profile is shown by the dotted line for comparison. It is evident that the size of the plateau around corotation decreases by at least a factor of 2 as compared to that in model 1. This effect can be understood if we consider the residual gas ve-

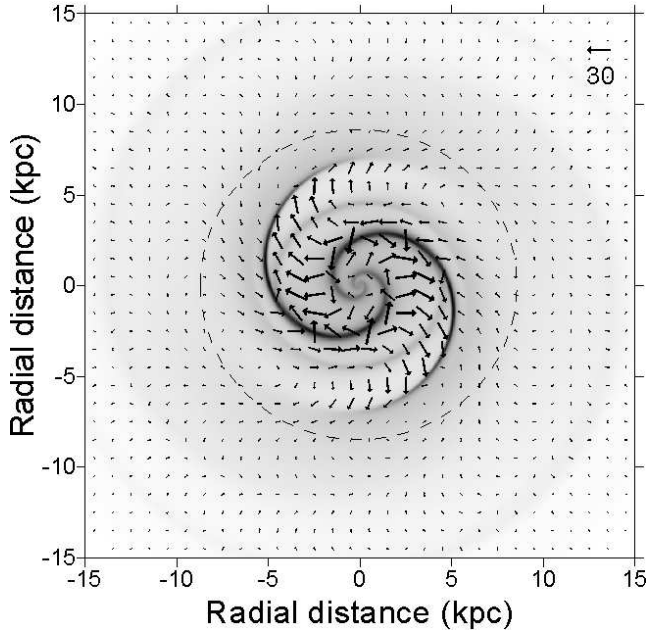


Figure 10. The residual gas velocity field superimposed onto the gas surface density distribution in model 2 at $t = 0.9$ Gyr. Corotation is drawn by the dashed circle. The scale vector is in km s^{-1} . Cyclones or anticyclones are hardly visible in the residual gas velocity field.

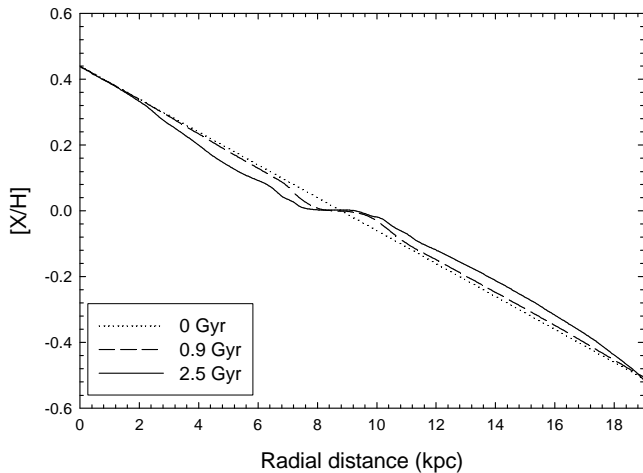


Figure 11. Azimuthally averaged abundance distribution of element X at three different times as indicated in the legend.

locity field shown in Fig. 12 for the model with $i = 10^\circ$. This velocity field is calculated in the same manner as in Sect. 5.1 and is superimposed on the gas surface density distribution at $t = 0.9$ Gyr. The position of corotation is drawn by the circle and the anticyclones are drawn by the ellipses. A comparison of Fig. 12 and Fig. 7 indicates that the anticyclone flows of gas are much less pronounced in tightly-wound galaxies with $i = 10^\circ$ than in galaxies with $i = 25^\circ$. The radial gas velocities and the overall extent of anticyclones are noticeably smaller in tightly-wound spirals. For instance, the maximum and average radial velocities around corotation in the $i = 25^\circ$ model 1 are $\pm(25-30) \text{ km s}^{-1}$ and $\pm(5-8) \text{ km s}^{-1}$, respectively. The inward radial velocities

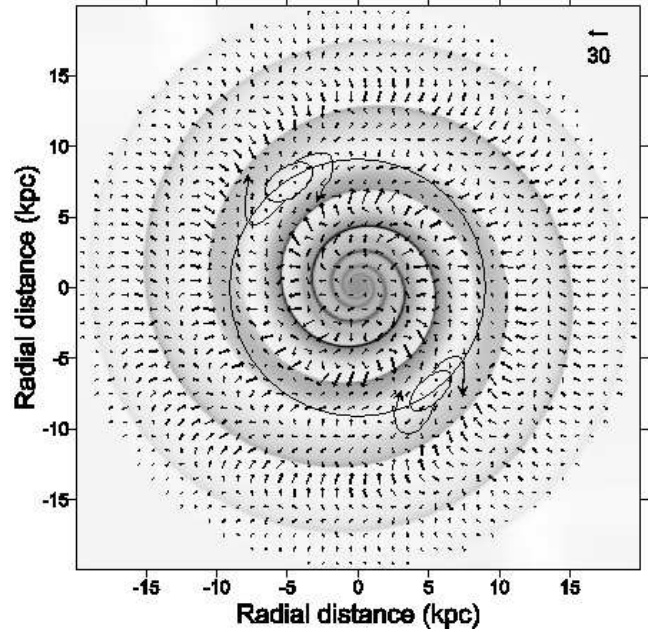


Figure 12. The residual gas velocity field superimposed onto the gas surface density distribution in the model with $i = 10^\circ$ at $t = 0.9$ Gyr. The locations of anticyclones are shown with the ellipses. Large arrows sketch the gas flow in anticyclones. Corotation is drawn by the circle. The scale vector is in km s^{-1} .

are usually larger than the outward ones by approximately 10% – 20%. On the other hand, in the $i = 10^\circ$ model with more tightly-wound arms the maximum and average radial velocities are $\pm(5-8) \text{ km s}^{-1}$ and $\pm(1-2) \text{ km s}^{-1}$, respectively. It is not surprising that the efficiency of radial redistribution of heavy elements and the sizes of plateaus around corotation are noticeably lower in the $i = 10^\circ$ model than in the $i = 25^\circ$ model 1.

The radial positions of a logarithmic stellar spiral at zero phase ($\phi = 0$, see eq. 8) can be determined as

$$r_n = r_{\text{sp}} \exp(2\pi n \tan(i)/m) \quad (11)$$

where $n = 0, \pm 1, \pm 2, \dots$ and $r_0 = r_{\text{sp}}$ is the characteristic radius of the stellar spiral at $\phi = 0$. Equation 11 becomes inapplicable when the separation between the gas spirals is considered, because there exist a non-negligible azimuthal phase shift between the stellar and gas spirals caused by the non-solid-body rotation curve of the gas disk. This phase shift is particularly large outside corotation where the gas rotation curve declines with radius. As a consequence, the separation between the gas spirals decreases considerably, especially in the case of larger pitch angles. Therefore, we use a visual estimate for the radial separation between the gas spirals.

Our numerical simulations indicate that the anticyclone flows are bounded by the adjacent gas spiral arms. This implies that the sizes of plateaus in the radial profiles of heavy elements should be proportional to the radial separation between the gas spiral arms on both sides of corotation. Indeed, a visual inspection of Fig. 7 and Fig. 12 indicates that the radial separation is at least a factor of 2 larger in the $i = 25^\circ$ model than in the $i = 10^\circ$ model. Consequently, the size of the plateau around corotation is also approximately

a factor of 2 larger in the $i = 25^\circ$ model. Hence, the radial separation between the gas spiral and an associated anticyclone activity is expected to increase along the Hubble sequence. It is now not surprising that both Grand-Design galaxies NGC 3631 and NGC 157, where giant anticyclones have been observed (Fridman et al. 2001a; 2001b), are of Sc and Sbc types, respectively. We conclude that plateaus in the radial abundance distribution of heavy elements have a tendency to increase in size along the Hubble sequence.

Two-armed spiral galaxies have been considered so far. In multi-armed galaxies ($m > 2$), the radial separation between the gas spiral arms is smaller than in two-armed galaxies with the same pitch angle. This should also reduce the sizes of anticyclones and the associated efficiency of radial heavy element redistribution. We leave this issue for a subsequent study.

7 SUMMARY

We have studied numerically the dynamics of warm gas and heavy elements in spiral galaxies. Two types of two-armed spiral galaxies are considered in which corotation is situated approximately in the middle of the spiral pattern (type 1) and at the very end of it (type 2), respectively. Type 2 spiral galaxies show little radial redistribution of heavy elements in the warm gas disk. Conversely, type 1 spirals are distinguished by a substantial radial redistribution of heavy elements around corotation.

Strong cyclones and anticyclones around corotation are generated by the non-axisymmetric gravitational field of spiral stellar density waves in type 1 galaxies. The anticyclone flows transport gas from inside corotation to the regions outside it and vice versa. If the radial abundances of heavy elements are characterized by a negative slope, the anticyclones bring many more atoms of heavy elements outside corotation than they import inside corotation. This results in a flattening of radial abundance profiles at the position of anticyclones after two revolution periods of a galaxy. On the other hand, the cyclone flows generate in-going and out-going streams of gas along the spiral arms. These streams meet at corotation, producing a contact discontinuity in the gas flow and associated step-like radial profiles of heavy element abundances at the position of cyclones. Nevertheless, the azimuthally averaged radial abundance distributions of heavy elements show *a well-defined plateau on both sides of corotation*, implying that anticyclones are more powerful in transporting the heavy elements than cyclones.

The sizes of plateaus around corotation in the azimuthally averaged radial abundance distributions of heavy elements are expected to increase along the Hubble sequence in spiral galaxies with equal number of arms. Our numerical simulations show that in two-armed Sa-Sb galaxies with a pitch angle of 10° , the plateau has a maximum size of 2 kpc. In contrast, Sc galaxies with a pitch angle of 25° have the plateau that can become as large as 4.5 kpc. A growing efficiency of radial mixing of heavy elements (and an associated flattening of negative abundance gradients) along the Hubble sequence is related to the increasing radial separation between the spiral arms and a consequent increase in the strength of anticyclones.

A considerable portion of total gas mass in a spiral

galaxy may be in the form of cold molecular hydrogen clouds. Our numerical simulations show that the efficiency of radial mixing grows as the gas temperature drops. A decrease in the restoring force of pressure gradients is responsible for this effect. However, our numerical hydrodynamics code is not appropriate for the modelling of molecular cloud dynamics, for which the sticky particle codes are well suited. Sellwood & Binney (2002) and Sellwood & Preto (2002) have employed N-body simulations to study the dynamics of cold molecular clouds. They have reported the development of anticyclonic motions at corotation and predicted the flattening of any metallicity gradients within the disc.

In this paper, we neglect the effect of continuous star formation. It is a computationally difficult task to self-consistently include the production of heavy elements in the hydrodynamics code. A possible exception is oxygen which is released mostly by short-living massive stars, for which the instantaneous recycling approximation can be used (e.g. Acharova et al. 2005). Our preliminary numerical simulations indicate that the on-going star formation in the spiral arms may change the shape of the plateau at corotation. More specifically, a mild minimum and maximum in the azimuthally averaged radial abundance profile of oxygen may develop at the inner and outer sides of corotation, respectively. Similar shapes in the radial abundance distribution of oxygen near corotation were reported by Acharova et al. (2005). The results of this study will be presented in a follow-up paper.

ACKNOWLEDGMENTS

The author is grateful to the referee, J. R. D. Lépine, for useful suggestions that helped to improve the final presentation. The author is also thankful to Shantanu Basu for help with English language usage and Yu. A. Shchekinov for valuable comments. Support from a CITA National Fellowship is gratefully acknowledged.

REFERENCES

- Acharova I. A., Lépine J. R. D., Mishurov Yu. N., 2005, MNRAS, 359, 819
- Andrievsky S. M., Luck R. E., Martin P., Lépine J. R. D., 2004, A&A, 413, 159
- Binney J., Tremaine S., 1987, Galactic Dynamics. Princeton Univ. Press, Princeton
- Daflon S., Cunha K., 2004, ApJ, 617, 1115
- Fridman A. M., Khoruzhii O. V., Lyakhovich V. V., Sil'chenko O. K., Zasov A. V., et al., 2001, A&A, 371, 538
- Fridman A. M., Khoruzhii O. V., Polyachenko E. V., Zasov A. V., Sil'chenko O. K., et al., 2001, MNRAS, 323, 651
- Hubble E. P., 1926, ApJ, 64, 321
- Kennicutt R. C., 1981, AJ, 86, 1847
- Lépine J. R. D., Acharova I. A., Mishurov Yu. N., 2003, ApJ, 589, 210
- Lin C. C., Yuan C., Shu F. H., 1969, ApJ, 155, 721
- Mishurov Yu. N., Lépine J. R. D., Acharova I. A., 2002, ApJ, 571, L113
- Nezlin M. V., 1994, in King I. R., ed., ASP Conference

Ser. Vol. 66, Physics of the Gaseous and Stellar Disks of the Galaxy, p. 135

Norman M. L., Wilson J. R., Barton R. T., 1980, *ApJ*, 239, 968

Sellwood J. A., Binney J. J., 2002, *MNRAS*, 336, 785

Sellwood J. A., Preto M., 2002, in Athanassoula E., Bosma A., eds, Disks of Galaxies. Kinematics. Dynamics and Perturbations. Astron Soc. Pac., San Francisco, 275, 281

Stone J., M., Norman M. L., 1992. *ApJS* 80, 753

Toomre A., 1963. *ApJ*, 138, 385

Vorobyov E. I., Shchekinov Yu. A., 2006, *NewA*, 11, 240

Zaritsky D., Kennicutt R. C. Jr., Huchra J. P., 1994, *ApJ*, 420, 87